Journal of Materials Chemistry A

Porous hollow α-Fe2O3@TiO2 core-shell nanospheres for superior lithium/sodium storage capability

Journal:	*Journal of Materials Chemistry A*
Manuscript ID:	TA-ART-04-2015-002994.R1
Article Type:	Paper
Date Submitted by the Author:	16-May-2015

Complete List of Authors:	Fu, Yanqing; Xiangtan University, school of chemistry Wei, Qiliang; Institut National de la Recherche Scientifique, Énergie Matériaux et Télécommunications Wang, Xianyou; Xiangtan University, school of chemistry shu, hongbo; Xiangtan University, school of chemistry yang, xiukang; Xiangtan University, shool of chemistry Sun, Shuhui; Institut National de la Recherche Scientifique , Energy and Materials

A table of contents entry:

graphic:

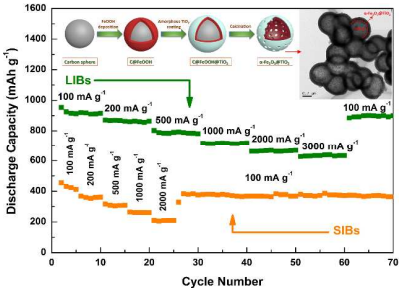

Text:

Porous hollow α-Fe_2O_3@TiO_2 core-shell nanospheres with hollow inner cavity and porous outer shell exhibits outstanding electrochemical properties for LIBs/SIBs.

Porous hollow α-Fe_2O_3@TiO_2 core-shell nanospheres for superior lithium/sodium storage capability

Yanqing Fu,[a] Qiliang Wei,[b] Xianyou Wang,[*a] Hongbo Shu,[a] Xiukang Yang,[a] Shuhui Sun[b]

[a]*Key Laboratory of Environmentally Friendly Chemistry and Applications of Ministry of Education，Hunan Province Key Laboratory for Electrochemical Energy Storage and Conversion，School of Chemistry, Xiangtan University, Hunan, Xiangtan 411105, China*

[b]*Institut National de la Recherche Scientifique –Énergie Matériaux et Télécommunications, Varennes, QC J3X 1S2, Canada*

Abstract: Porous hollow α-Fe_2O_3@TiO_2 core-shell nanospheres for using as anode material for lithium-ion batteries (LIBs) and sodium-ion batteries (SIBs) have been successfully fabricated by a simple template-assisted method, which has been rarely reported before. The scanning electron microscopy (SEM), transmission electron microscopy (TEM) and N_2 adsorption-desorption isotherm reveal that the as-prepared α-Fe_2O_3@TiO_2 is composed of hollow inner cavity and outer shell with massive mesopores. This porous hollow structure is capable of buffering the large volume variation of α-Fe_2O_3 during cycling and preventing the electrode from pulverization and aggregation, as well as providing sufficiently large interstitial space within crystallographic structure to host alkalis (Li and Na). As a consequence, this hybrid composite exhibits outstanding electrochemical properties, e.g., high specific capacity, excellent cyclability, satisfactory rate performance, and splendid initial coulombic efficiency for both LIBs and SIBs.

[*]**Corresponding author:** Xianyou Wang Tel: +86 731 58292060; fax: +86 731 58292061.
E-mail address: wxianyou@yahoo.com (X. Wang).

Keywords: Anode material; Lithium-ion batteries; Sodium-ion batteries; Electrochemical properties; Porous hollow structure

1. Introduction

It is universally acknowledged that rechargeable lithium-ion batteries (LIBs) have been the most utilized batteries in both stationary and portable electronic market for many years, with the advantages of high energy density, long lifespan, high operating voltage and environmental benignity.[1-5] Recently, sodium-ion batteries (SIBs) have also been thought to be very attractive for applications in large-scale stationary energy storage and smart grids, driven by the abundant Na resources and their potentially low cost in raw materials, as well as the increasing demand of renewable green energy.[6-8] Hence, a great deal of interest has been boosted in seeking for high-performance electrode materials with the capability to store and deliver more energy efficiently for both LIBs and SIBs. With regard to transition metal oxides (TMOs), hematite (α-Fe_2O_3) has always been regarded as a very appealing anode candidate because of its much higher theoretical capacity (1007 mA h g^{-1} in LIBs) than that of conventional graphite (372 mA h g^{-1}), as well as nontoxicity, high corrosion resistance and low processing cost.[9-11] Despite of these attractive features, α-Fe_2O_3 inevitably suffers from large irreversible capacity loss, low initial coulombic efficiency, poor rate capability and cycling stability due to their drastic volume variation and severe destruction of the electrode during the repeated charge/discharge process.[12]

So far, an enormous amount of efforts have been devoted to solve these thorny

problems. Thereinto, hollow structures with high surface area, good permeation and high loading capacity have attracted considerable attention as an important solution in recent years.[13-15] It is true that not only porous hollow structure reduces effective diffusion distance for Li^+/Na^+, but also buffers against the local volume change during lithium/sodium insertion/extraction under certain conditions. Nonetheless, in most cases, without any coating they still exhibit capacity fading during cycling due to their intrinsically poor electrical conductivity and/or inappropriate wall thickness. For instance, Xiao et al.[16] fabricated hollow α-Fe_2O_3 microcubes by a facile hydrothermal method in an ethanol-water co-solvent system, the reversible capacity gradually decreased from 1522 to 457 mA h g^{-1} at a current density of 100 mA g^{-1} after 100 cycles. In this regard, assembly of various metal oxides into a hierarchical nanocomposite with core-shell structure is a feasible strategy, which has already been introduced to high-performance materials in LIBs, such as Fe_2O_3/SnO_2,[17] Fe_2O_3/Co_3O_4,[18] Fe_2O_3/PANI,[19] Fe_2O_3/β-MnO_2,[20] Fe_2O_3/TiO_2,[21] and so on. However, rational design and synthesis of this kind of material is still a great challenge due to the complexity of the interactions between the components and their influence on the lithium/sodium storage properties.

It is well known that TiO_2 is an excellent anode material with attractive properties, including low cost, abundant resources, environmental friendliness, and little volume variation as a result of its layered crystalline structure.[22] Compared with traditional carbon coating, it is an active Li/Na host with high theoretical capacity. [23] Accordingly, it is of great value to make rationally use of TiO_2 as the coating layer to

alleviate the volume expansion of α-Fe_2O_3 and provide a highway for charge transfer. However, to the best of our knowledge, there is still no report on Fe_2O_3/TiO_2 porous hollow nanostructure as high performance anodes for both LIBs and SIBs.

Herein, combining the advantages of the porous hollow structure and the assembly of different metal oxides design, as well as considering an effective method which is simple and can be scaled up, we report a carbon-template assisted synthetic approach for the preparation of porous hollow α-Fe_2O_3@TiO_2 nanospheres for LIBs and SIBs. Since the synthesis route (as illustrated in Scheme 1) is advantageous for its narrow size distribution, ready availability in relatively large amounts, feasibility of a wide range of sizes, and simplicity of its synthesis, it is practical and also applicable to other materials, such as TiO_2, SnO_2…, even involving multiple steps. This configuration of α-Fe_2O_3@TiO_2 hybrid composite not only provides extra space for the storage of Li^+/Na^+ and reduces effective diffusion distance for Li^+/Na^+ by the void space in hollow structure, but also accommodates variation in the volume of α-Fe_2O_3 and prevents α-Fe_2O_3 from pulverization and aggregation via the TiO_2 layer. This novel structure exhibits outstanding electrochemical performance with satisfactory cyclability and excellent rate capability in comparison to those of bare hollow α-Fe_2O_3 spheres. The physicochemical and electrochemical properties of the as-prepared α-Fe_2O_3@TiO_2 composite are studied in detail.

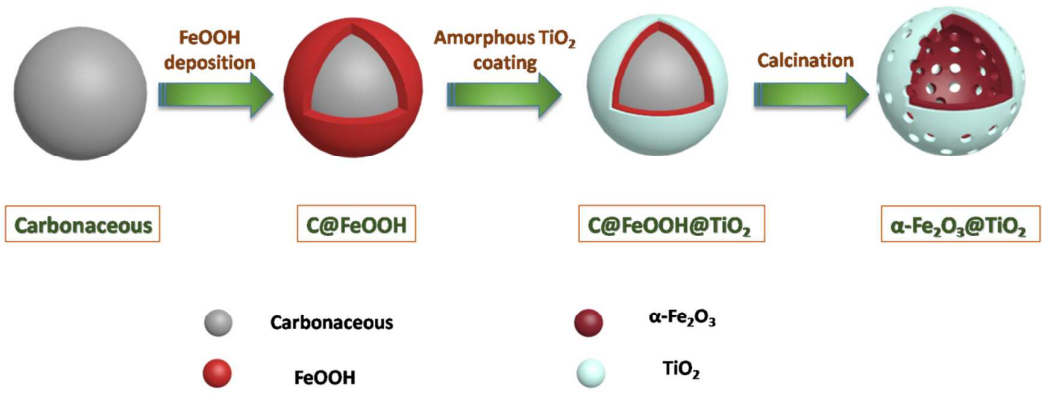

Scheme 1 Schematic illustration of the synthetic process for porous hollow α-Fe_2O_3@TiO_2 core-shell spheres.

2. Experimental

2.1 Synthesis of carbonaceous (C) spheres

All the reactants below were of analytical grade and used without further purification. In a typical synthesis, 6.93 g $C_6H_{12}O_6 \cdot H_2O$ was dissolved into 70 mL distilled water under magnetic stirring until it was completely dissolved. Then, the glucose solution was transferred to a 100 mL Teflon autoclave, sealed and maintained at 180 °C for 6 h in an oven. After cooling down to room temperature, the dark-brawn product was collected by centrifugation and then washed with deionized water and absolute ethanol for several times respectively, followed by drying at 70 °C for 12 h in an oven.

2.2 Synthesis of α-Fe_2O_3@TiO_2 hollow spheres

The synthetic route consists of two steps.

(1) 10 mL deionized water and 50 mL absolute ethanol were mixed together, then 3.24 g $FeCl_3 \cdot 6H_2O$, 1.8 g urea and 0.3 g as-prepared C were added into the solution under stirring. After stirring to form a homogeneous solution, the mixture was kept at

70 °C for 48 h without stirring. After reaction, the precipitate (named product 1) was collected by centrifugation and then washed with deionized water and absolute ethanol for several times respectively, followed by drying at 80 °C for 10 h in an oven.

(2) 0.25 g product 1 was dispersed into 100 mL absolute ethanol and mixed with concentrated ammonia solution (0.15 mL, 28 wt%) under 30 min sonication. Afterward, 0.30 mL of TBOT was dropwise added within 5 min, and the reaction was allowed to proceed for 24 h at 45 °C under mechanical stirring. The precipitate was collected by centrifugation and then washed with deionized water and absolute ethanol for several times respectively, followed by drying at 80 °C for 10 h in an oven. Finally, the desiccated material was heated in a quartz tube to 500 °C in air at a rate of 5 °C min^{-1} and kept at this temperature for 2 h to obtain hollow α-Fe_2O_3@TiO_2 spheres.

For comparison, the hollow α-Fe_2O_3 sphere was prepared by directly annealing product 1 with the same condition, and the bare TiO_2 was synthesized by step 2 without the addition of product 1.

2.3 Physical characterizations

The X-ray powder diffraction (XRD) was carried out by a Rigaku D/MAX-2500 powder diffractometer with a graphite monochromator and Cu Kα radiation (λ = 0.15418 nm) operated at a scan rate of 10° min^{-1} in the 2θ range of 10°-80°, with a step size of 0.02°. Scanning electron microscopy (SEM) images were collected using a JEOL JSM-6610 scanning electron microscope. The field-emission scanning

electron microscopy (FESEM, Nova NanoSEM 230) was used to understand the morphology and structure of samples. Transmission electron microscopy (TEM) and high-resolution TEM (HRTEM) observations, as well as energy dispersive X-ray spectroscopy (EDS) analyses were obtained using a JEOL JEM-2100F transmission electron microscope at an acceleration voltage of 200 kV. The specific surface area of the as-prepared sample was determined by N_2 adsorption/desorption isotherm at 77 K (JW-BK112), and the pore size distribution stem from the adsorption branch of isotherms based on the Barrette-Joynere-Halenda (BJH) model. The value state of chemical composition was detected via X-ray photoelectron spectroscopy (XPS) with a K-Alpha 1063 using mono Al Kα (Thermo Fisher Scientific, UK). The chemical composition of sample was confirmed by atomic absorption spectroscopy (AAS, Vario 6 Analytik Jena AG, Jena).

2.4 Electrochemical Measurements

The button-type cells were assembled in an argon-filled glove box, where water and oxygen concentration were kept less than 5 ppm. The working electrodes were fabricated by mixing 70 wt% of active materials, 20 wt% of acetylene black and 10 wt% of polymer binder (polyvinylidene fluoride, PVDF), which were then pasted on copper foil followed by drying under vacuum at 110 °C for 10 h. The active material loading in each electrode disc (about 10 mm in diameter) is typically 1.5-2 mg, corresponding to about 1.9-2.5 mg cm^{-2}. For lithium cell, lithium disc was served as both counter electrode and reference electrode; 1 M $LiPF_6$ in a mixture of ethylene carbonate (EC) and edimethyl carbonate (DMC) (1:1, V/V) was used as an electrolyte

and the separator was Celgard 2400. For sodium cell, metal sodium was used as negative electrode; the electrolyte was 1 M $NaClO_4$ in propylene carbonate (PC) solution; the separator was glass microfiber filters (Whatman, GF/D). The galvanostatic charge-discharge measurements were performed using a Neware battery tester BTS-XWJ-6.44S-00052 (Neware, Shenzhen, China) at different current densities with a cut-off voltage window of 0.01-3.0 V. The calculation of the specific capacity is based on the overall mass of the composite synthesized. Cyclic Voltammetry (CV) tests were carried out on VersaSTAT3 electrochemical workstation (Princeton, America) at a scan rate of 0.1 mV s^{-1} with the potential interval 0.01-3.0 V. Electrochemical impedance spectroscopy (EIS) was also performed using VersaSTAT3 electrochemical workstation by applying an Ac amplitude of 5 mV over the frequency range from 10^5 to 0.01 Hz. All the electrochemical measurements were performed at room temperature.

3. Results and discussion

3.1 Structural and morphology analysis

The phase composition and structures of the as-prepared samples were identified by X-ray powder diffraction (XRD). As shown in Fig. 1a and b, all peaks indicated by Miller indices for the as-synthesized TiO_2 and hollow α-Fe_2O_3 are in good agreement with the standard XRD patterns of tetragonal anatase TiO_2 (JCPDS No. 21-1272) and rhombohedral α-Fe_2O_3 (JCPDS No. 33-0664), respectively. Particularly, Fig. 1c is the XRD pattern of this porous hollow structure, in which all the diffraction peaks can be well indexed to tetragonal anatase TiO_2 and hexagonal α-Fe_2O_3, no additional peaks

were found, demonstrating a successful combination of TiO_2 and α-Fe_2O_3. The structure sketches for TiO_2 and α-Fe_2O_3 are respectively shown in Fig. 1d and e. Thereinto, the TiO_2 structure consists of edge-sharing TiO_6 octahedrons with a great deal of empty zigzag channels, which is beneficial for the introduction and fast diffusion of alkalis (Li and Na) through the (001) facets,[24] the unit cell of α-Fe_2O_3 composed of FeO_6 octahedrons stacking forms the hexagonal close-packed structure without any interlayer spacing and tunnels.[25]

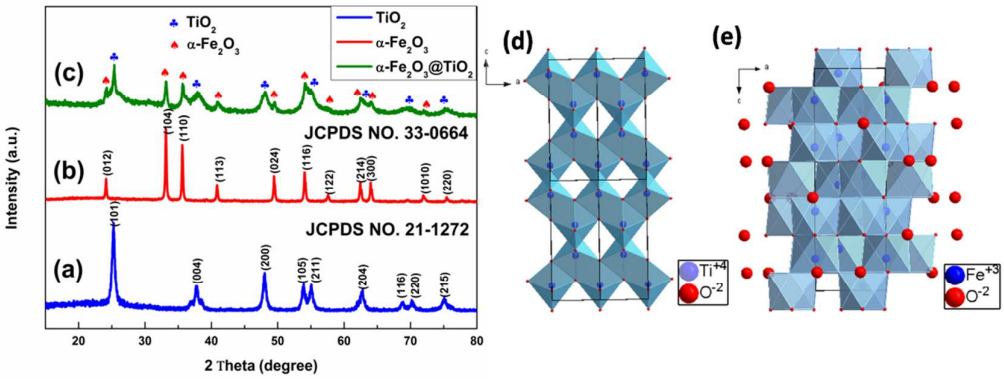

Fig. 1 XRD patterns of (a) TiO_2, (b) α-Fe_2O_3 and (c) α-Fe_2O_3@TiO_2. Cell structures of (d) tetragonal TiO_2 and (e) hexagonal α-Fe_2O_3 along the direction of [010].

X-ray photoelectron spectroscopy (XPS) was conducted to further characterize the chemical compositions and metal oxidation states of the α-Fe_2O_3@TiO_2 hybrid composite. The corresponding XPS spectra of C 1s, O 1s, Fe 2p and Ti 2p are displayed in Fig. 2. As shown in Fig. 2a, the peak of C 1s spectrum at 284.4 eV is attributed to benchmark carbon.[26] Meanwhile, as for the O 1s spectrum, the peak at 529.4 eV results from that the O^{2-} forming oxides with Ti and Fe.[27] For Fe 2p spectrum (Fig. 2c), there are two distinct peaks at 710.9 eV and 724.5 eV, which are respectively corresponded to Fe $2p_{2/3}$ and Fe $2p_{1/2}$ of α-Fe_2O_3. Furthermore, two

satellite peaks located on 719.5 and 734.0 eV are also in accordance with the electronic state of α-Fe_2O_3.[28] In terms of the Ti 2p spectrum (Fig. 2d), two peaks settle in 459.8 and 465.5 eV driving from Ti $2p_{3/2}$ and Ti $2p_{1/2}$, respectively; the spin energy separation between the Ti $2p_{1/2}$ and Ti $2p_{3/2}$ core levels is 5.7 eV, suggesting a normal state of Ti^{4+} in the anatase TiO_2.[29, 30]

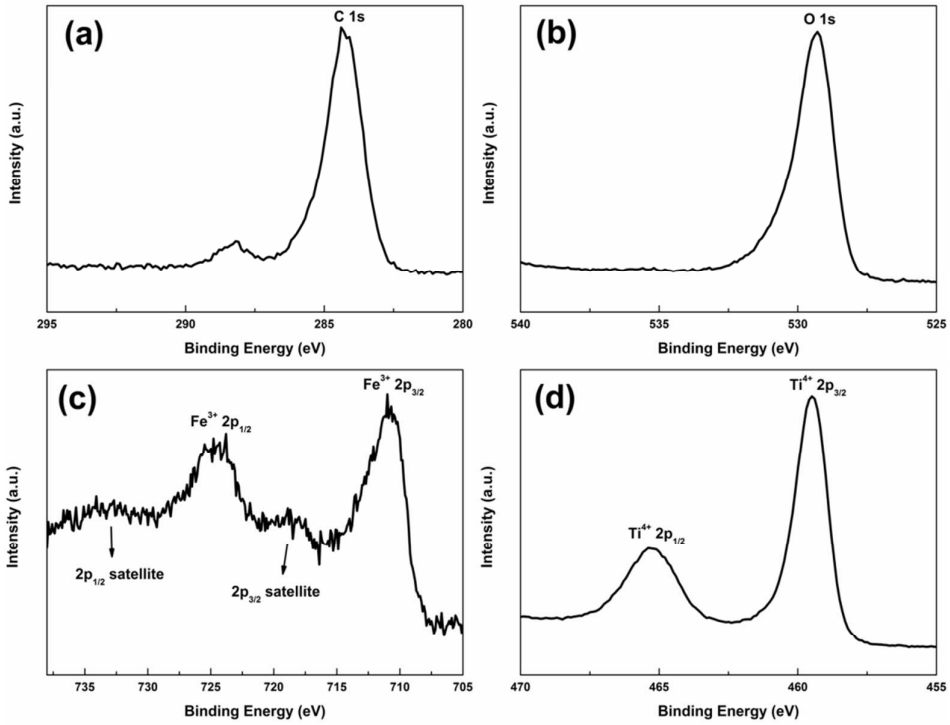

Fig. 2 XPS core level spectra of (a) C 1s, (b) O 1s, (c) Fe 2p and (d) Ti 2p for α-Fe_2O_3@TiO_2.

The morphological and structural features of the as-prepared α-Fe_2O_3@TiO_2 and α-Fe_2O_3 were respectively characterized by filed-emission scanning electron microscopy (FESEM) and scanning electron microscopy (SEM). From Fig. 3a and b, it can be clearly seen that the structure of α-Fe_2O_3 is hollow sphere with a size of 300-500 nm, and it displays a matte surface. Lots of crushed material can also be observed around the α-Fe_2O_3 hollow spheres. After coating TiO_2 (Fig. 3c and d), the presence of smooth surface with hollow structure for α-Fe_2O_3@TiO_2 is obviously

represented, indicating TiO_2 layer forming via tiny particles is closely deposited on the surface of α-Fe_2O_3. According to the atomic absorption spectroscopy (AAS), the chemical composition of α-Fe_2O_3@TiO_2 hybrid is detected with ~70.6 wt% α-Fe_2O_3 and ~29.4 wt% TiO_2.

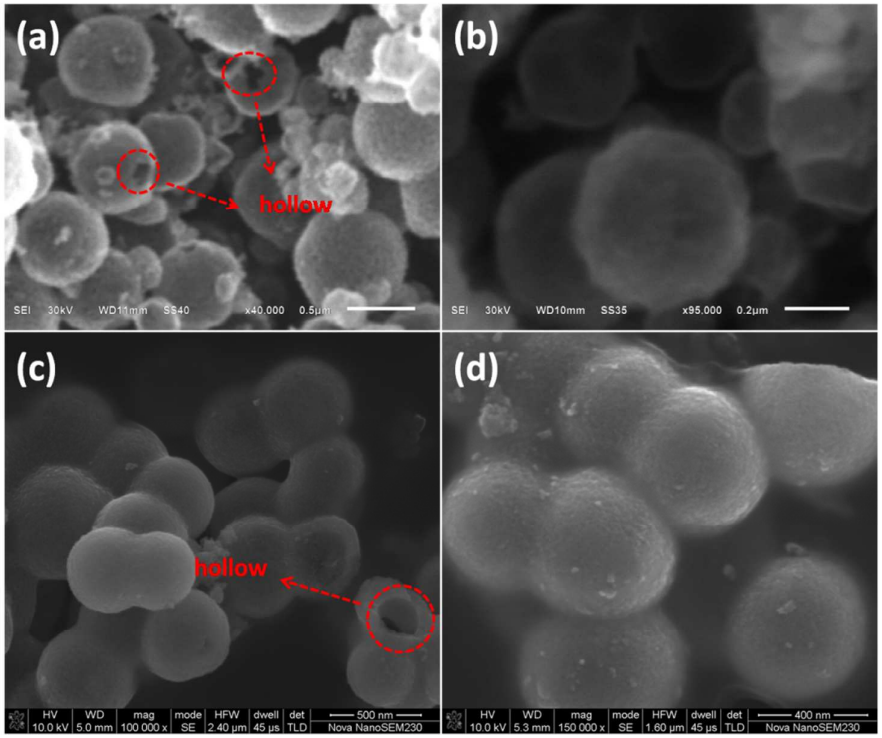

Fig. 3 SEM images (a and b) of α-Fe_2O_3 and FESEM images (c and d) of α-Fe_2O_3@TiO_2.

More detailed structural characteristics for as-obtained samples were supported by transmission electron microscopy (TEM). As shown in Fig. 4a, a large number of small nanoparticles accumulate into α-Fe_2O_3 hollow spherical structure with a shell thickness of ~50 nm; some broken materials can be apparently observed in the case without the TiO_2 protection layer, which is consistent with SEM. The lattice spacing of 0.37 nm and the selected area fast Fourier transformation (FFT) image (inset) in Fig. 4b are assigned to the (012) plane of α-Fe_2O_3.[31] A typical TEM in Fig. 4c presents the presence of porosity, hollow sphere (diameter of 300-600 nm) and relative smooth

surface of α-Fe_2O_3@TiO_2, along with a shell thickness of ~70 nm, revealing almost no change in its overall morphology in comparison to that of α-Fe_2O_3. Moreover, from the high resolution TEM (HRTEM) image shown in Fig. 4d, the lattice fringe spacings of 0.35 nm correspond to the (101) plane of anatase TiO_2,[32] and the inset displays a clear interface region and good connection between α-Fe_2O_3 and TiO_2. Consequently, the TiO_2 is successfully and uniformly attached to the core of α-Fe_2O_3. The energy dispersive X-ray spectroscopy (EDS) in Fig. 5a shows the presence of Ti element, further indicating the successful TiO_2 coating on the surface of α-Fe_2O_3. More interestingly, as shown in Fig. 4e and f, numerous uniform mesopores (2-6 nm) in the outer shell probably arising from the escape of CO_2 during calcination and the voids between aggregated TiO_2 nanocrystals, result in a higher surface area. This texture characteristic of α-Fe_2O_3@TiO_2 was further confirmed by N_2 adsorption/desorption isotherm measurement (carried out at 77 K) shown in Fig. 5b. From the N_2 sorption data, the Brunauer-Emmett-Teller (BET) surface area is conducted as high as 174.4 m^2 g^{-1}, and the corresponding Barrette-Joynere-Halenda (BJH) pore-size distribution (inset) is mainly in the range of 2-6 nm with the mean pore diameter of 3.196 nm. This hollow structure with abundant mesopores and stable shell of TiO_2 is likely to buffer the volume expansion and allow the penetration of electrolyte to completely contact with the active material, thus playing an important role in improving electrochemical properties of α-Fe_2O_3@TiO_2.

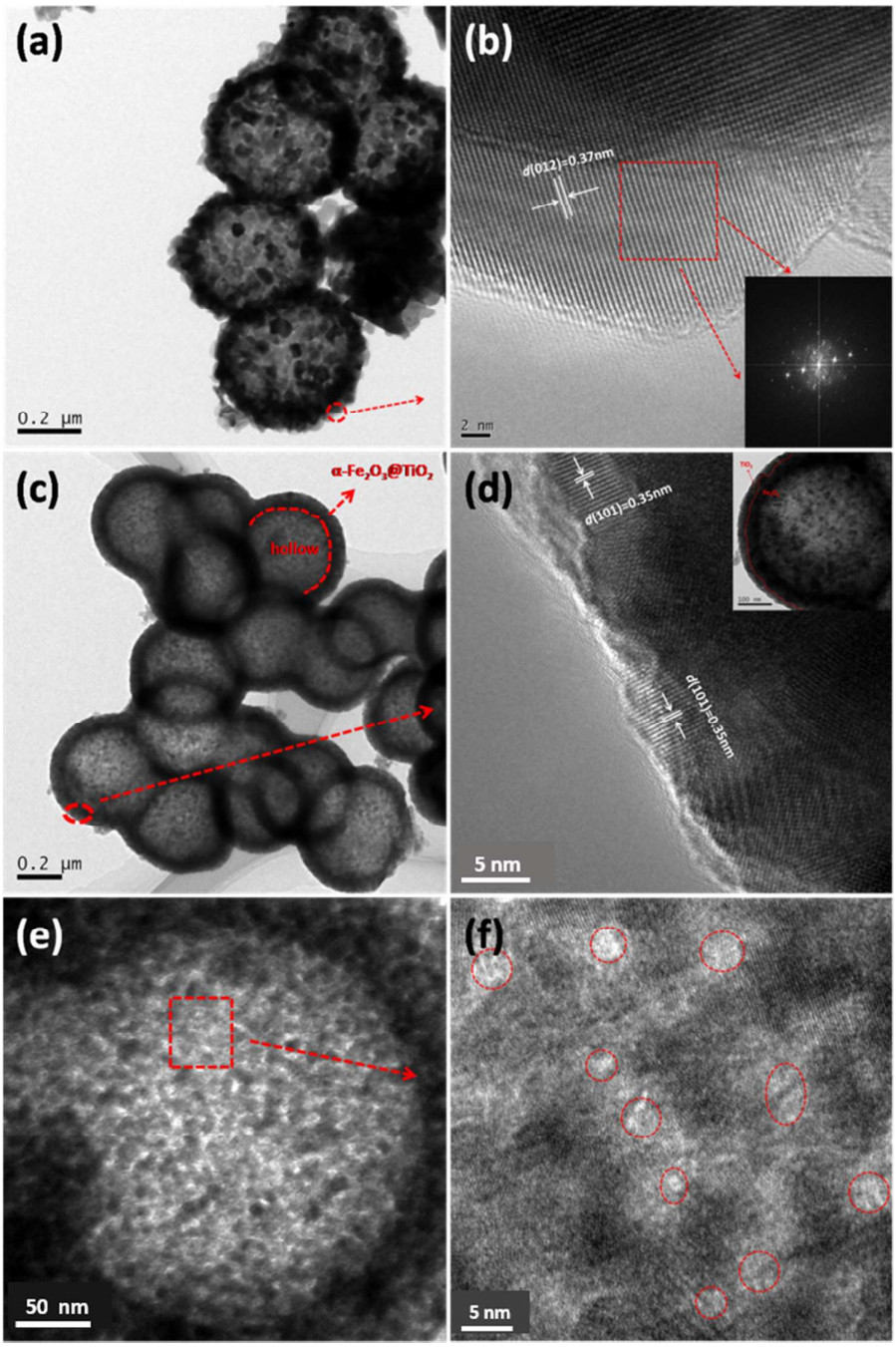

235

236 **Fig. 4** TEM images of (a, b) α-Fe_2O_3 and (c-f) α-Fe_2O_3@TiO_2 with different magnifications.

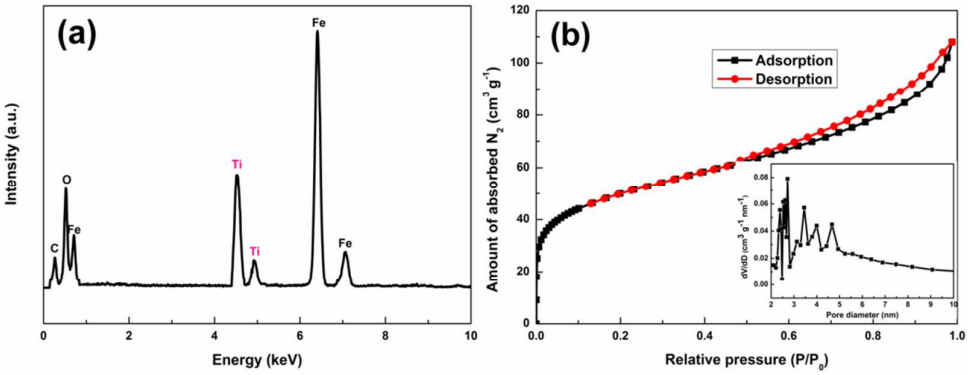

Fig. 5 EDS (a) and N_2 adsorption/desorption isotherms with pore-size distribution (inset) (b) of α-Fe_2O_3@TiO_2.

3.2 Electrochemical analysis of lithium ion batteries

In order to thoroughly elucidate the improved electrochemical performance for α-Fe_2O_3@TiO_2 electrode, the electrochemical properties with respect to Li insertion/extraction were investigated. Fig. 6 displays cyclic voltammetric (CV) curves for the three electrodes between 0.01 and 3.0 V at a scan rate of 0.1 mV s^{-1} so as to understand the reactive process. Fig. 6a and c present CVs of the as-prepared α-Fe_2O_3 and TiO_2, respectively, which are in good agreement with that of previously reported typical α-Fe_2O_3[29, 33, 34] and TiO_2[35, 36]. It is worth noting that the CV curves of TiO_2 repeat themselves well during cycles, while that of α-Fe_2O_3 are seriously shrinking. With regard to α-Fe_2O_3@TiO_2 (Fig. 6e), in the first cycle, the main cathodic peaks positioned at ~1.23 V and ~0.76 V are respectively ascribed to Eq. 1 and 2 with the process of electrolyte degradation (i.e., the solid electrolyte interphase (SEI) formation), indicating a two-step reduction process.

$$Fe_2O_3 + 2Li^+ + 2e^- \rightarrow Li_2(Fe_2O_3) \quad (1)$$

$$Li_2(Fe_2O_3) + 4Li^+ + 4e^- \rightarrow 2Fe^0 + 3Li_2O \quad (2)$$

$$Fe_2O_3 + 6Li \leftrightarrow 2Fe + 3Li_2O \quad (3)$$

$$TiO_2 + xLi^+ + xe^- \leftrightarrow Li_xTiO_2 \quad (4)$$

Besides, a pair of redox peaks at 1.73 V/2.11 V are observed, which are assigned to the solid-state Li diffusion of anatase TiO_2,[35, 36] as expressed in Eq. 4, suggesting a successful TiO_2 coating. According to previous research results[29, 33, 34] and our work (Fig. 6a), a broad and weak anodic peak of α-Fe_2O_3 can be observed at ~1.6-2.0 V. Presumably, due to the steep oxidation peak of TiO_2 is also positioned at ~2.1 V and too strong, the peak of α-Fe_2O_3 positioned at the same place is inevitably covered by it. Additionally, the anodic peak of α-Fe_2O_3 in the hybrid composite corresponds to the reversible oxidation of Fe^0 to Fe^{3+}.[37] Therefore, the overall electrochemical reactions of α-Fe_2O_3@TiO_2 are given in Eq. 3 and 4. On account of the polarization of active materials and the formation of SEI film in the first cycle, all the cathodic and anodic peaks are slightly shifted, and the peak intensities decrease during subsequent cycles. Obviously, the CV curves of α-Fe_2O_3@TiO_2 electrode (Fig. 6e) overlap reasonably well after the first cycle, demonstrating a high reversibility of the electrochemical reaction, and good cycling performance as discussed below.

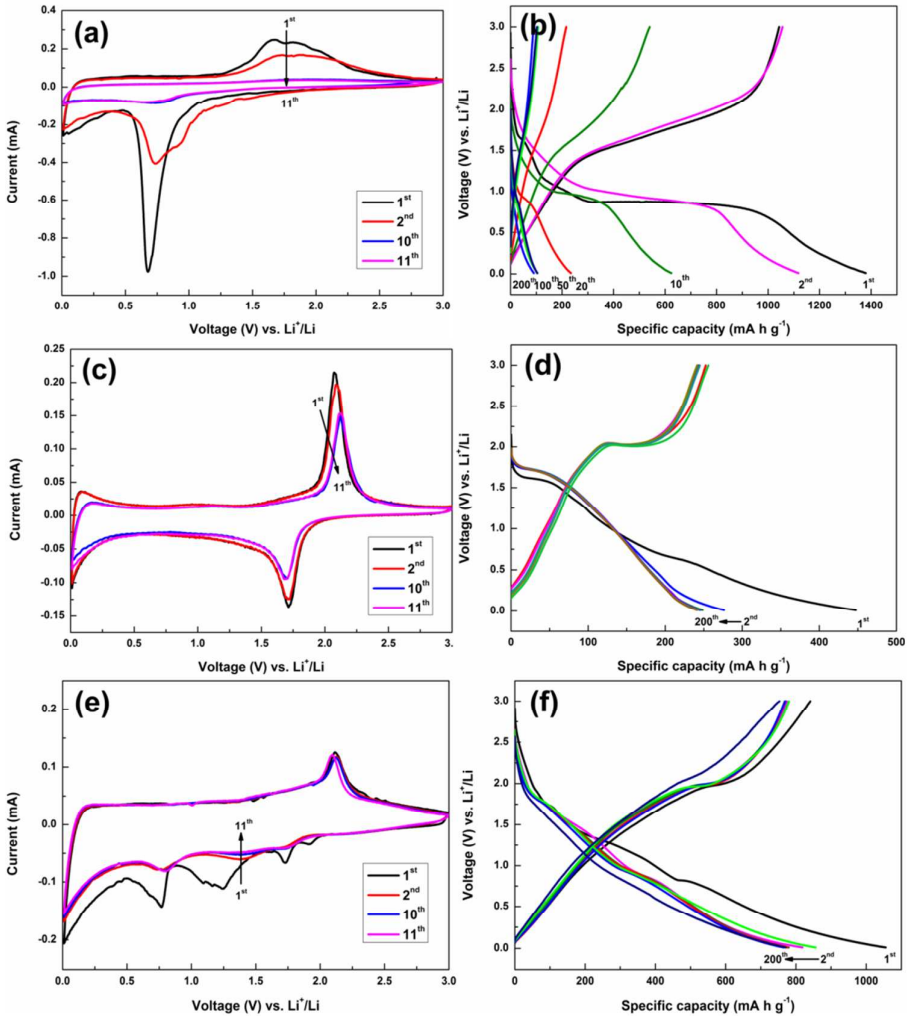

Fig. 6 CV curves and charge-discharge profiles of (a, b) α-Fe_2O_3, (c, d) TiO_2 and (e, f) α-Fe_2O_3@TiO_2 between 0.01 and 3.0 V at a scan rate of 0.1 mV s^{-1}.

The charge-discharge profiles for the three electrodes with a current density of 200 mA g^{-1} up to 200 cycles are also shown in Fig. 6. In Fig. 6f, during the first discharge process, there are three apparent voltage plateaus appear at ~0.8, ~1.25 and ~1.75 V, resulting from the lithium reactions with α-Fe_2O_3 (~0.8, ~1.25 V) and TiO_2 (~1.75 V), which are in good agreement with the CV results. Although the initial discharge capacity of α-Fe_2O_3@TiO_2 (1165 mA h g^{-1}, Fig. 6f) is slightly lower than that of α-Fe_2O_3 (1381 mA h g^{-1}, Fig. 6b), the stability of α-Fe_2O_3@TiO_2 is much better

than the latter. As can be seen from Fig. 6f, the discharge capacity (864 mA h g^{-1}) of α-Fe_2O_3@TiO_2 electrode in the 200th cycle is close to that of the 2nd cycle, showing good cycling stability and highly reversible process. In contrast, the discharge capacity of α-Fe_2O_3 (Fig. 6b) has an obvious decay during subsequent cycles, with only 100 mA h g^{-1} retained in the 200th cycle. Accordingly, TiO_2 in the composite not only alleviates the pulverization and drastic volume variation of the α-Fe_2O_3, but also offers the interstitial sites and suitable sized pathways for Li in the hybrid composite, which acts as a stable membrane for the Li^+ insertion/extraction processes and will thus facilitate the reversible Li^+ intercalation/deintercalation.

Fig. 7a compares the cycling performance of the three samples at 200 mA g^{-1} in the voltage range of 0.01-3.0 V. The corresponding coulombic efficiencies (CEs) are presented in Fig. 7b. It is obvious that the α-Fe_2O_3@TiO_2 in Fig. 7a displays good cycling performance and an excellent reversible specific capacity of 864 mA h g^{-1} up to 200 cycles, with an initial CE of 75.7% (which is significantly higher than that of α-Fe_2O_3 (60.4%) and TiO_2 (63.7%), as shown in Fig. 7b). The capacity of α-Fe_2O_3@TiO_2 electrode slightly decreases in the initial cycles, which is mainly ascribed to the formation of the SEI film. Besides, the additional TiO_2 will consume Li to form the Li_xTiO_2 compound. However, during the subsequent cycles, the exterior TiO_2 shell can effectively prevent the dissolution and mechanical failure of α-Fe_2O_3 particles, and it is also transformed to Li_xTiO_2, where the Ti^{3+} in Li_xTiO_2 is expected to enhance the overall conductivity of the electrode, thus leading to the capacity increase. Such a phenomenon has also been observed in other reports. [21, 38-40]

On the contrary, without the protection of TiO_2 shell, the hollow α-Fe_2O_3 suffers a fast capacity fading and only 100 mA h g^{-1} remained after 200 cycles. Moreover, compared to the CEs of α-Fe_2O_3 and TiO_2, that of α-Fe_2O_3@TiO_2 is slightly higher during cycling. Table 1 summarizes some recent works on the α-Fe_2O_3-based materials as anodes for LIBs. It has been found that the CE (75.7%) in this work is the best and the cycling performance of the α-Fe_2O_3@TiO_2 composite is superior to most of the previously reported results. Specifically, compared with the carbon-coated α-Fe_2O_3 composites,[38-40, 43-45] the electrochemical performance of the α-Fe_2O_3@TiO_2 composite in our work is much better. It can be ascribed to the special and stable crystallographic structure of TiO_2 which alleviates the volume expansion. Moreover, the formation of Li_xTiO_2 is able to enhance the overall electrical conductivity. In the same time, TiO_2 is also an active Li/Na host with relatively high theoretical capacity.

Table 1 Comparison of the recent work on α-Fe_2O_3-based materials as anodes for LIBs.

Sample	Current density/mAg^{-1}	Cycle number	Capacity/$mAhg^{-1}$ after cycles	Initial CE/%	Ref.
Core-shell α-Fe_2O_3/SnO_2 Heterostructures	100	30	341	68.7	41
Branched α-Fe_2O_3/SnO_2 nanoheterostructure	1000	30	260	69.4	17
α-Fe_2O_3@TiO_2 micro-ellipsoids	500	50	162.7	44.7	42
Porous α-Fe_2O_3@TiO_2 nanorods	100	46	449.3	60	21
α-Fe_2O_3@C/GNs hybrid	200	50	900	71	43
Rattle-type α-Fe_2O_3/C spheres	710	—	692	70.6	44

Hollow α-Fe_2O_3/PANI spheres	100	100	893	73.5	19
Bubble-nanorod-structured Fe_2O_3-C nanofibers	1000	300	812	69	45
SnO_2-Fe_2O_3@C composite	200	70	965	64	38
Fe_2O_3/C 3D electrode	4000	500	804.6	41.6	39
Carbon-coated α-Fe_2O_3 composite	500	300	1138	73.8	40
Thin triple-shell α-Fe_2O_3 hollow microspheres	50	50	1702	~73	46
Hollow α-Fe_2O_3@TiO_2 hybrids	200 2000	200 210	864 700	75.7 70.5	This work

In addition to the high capacity and much improved cycling performance, the α-Fe_2O_3@TiO_2 also exhibits significantly enhanced rate performance compared with the hollow α-Fe_2O_3 and bare TiO_2. As shown in Fig. 7c, all of the electrodes were firstly cycled at 100 mA g^{-1}, and irreversible capacity losses during the initial two cycles are clearly observed, which is probably owing to the decomposition of electrolyte and/or solvent. However, on account of the structural stability and the 3D network crystallographic structure of TiO_2 with empty zigzag channels, the α-Fe_2O_3@TiO_2 shows more stable reversible capacity than that of α-Fe_2O_3, as well as higher specific capacity than that of TiO_2 at various current densities. Even though they are cycled at a high current density of 3000 mA g^{-1}, the α-Fe_2O_3@TiO_2 still maintains a good reversible discharge capacity of 632 mA h g^{-1}, showing much higher rate capability than that of α-Fe_2O_3 (140 mA h g^{-1}) and TiO_2 (120 mA h g^{-1}). When the current density finally returns to its initial value of 100 mA g^{-1}, the capacity of 895

mA h g^{-1} still can be restored for α-Fe_2O_3@TiO_2, but, only 470 and 240 mA h g^{-1} for α-Fe_2O_3 and TiO_2, respectively. Specifically, even the α-Fe_2O_3@TiO_2 electrode cycled with a quite high current density of 2000 mA g^{-1} over 210 cycles (see in Fig. 7d), it still delivers an expected capacity of ~700 mA h g^{-1}. The improved rate performance is mainly ascribed to the formation of the TiO_2 layer via tiny particles with numerous uniform mesopores (2-6 nm) which provides a short diffusion path for electron/ion transfer, a large electrode-electrolyte contact area, and interior free space to alleviate pulverization strain. Moreover, Li can insert into TiO_2 crystal when it is discharged at 1.7 V, thus leading to the formation of the lithiated TiO_2 compound, Li_xTiO_2, where the Ti^{3+} in Li_xTiO_2 is expected to enhance the overall conductivity of the electrode. [23, 47] In other words, such excellent electrochemical performance is a manifesto of the advantage of the rationally designed porous hollow nanostructure, as well as the synergistic effects of the multiple functions of α-Fe_2O_3 and TiO_2.

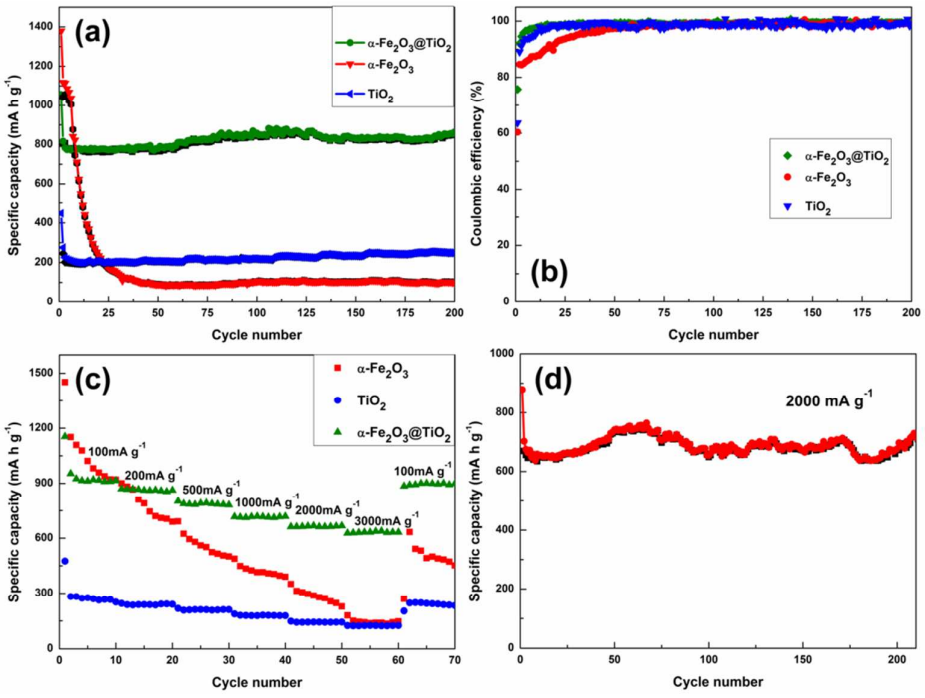

Fig. 7 Cycling performance and coulombic efficiencies of (a) TiO_2, (b) α-Fe_2O_3 and (c) α-Fe_2O_3@ TiO_2 at 200 mA g^{-1}. (c) Rate performance of the three electrodes at various current densities from 100 to 3000 mA g^{-1}. (d) Cycling performance of α-Fe_2O_3@ TiO_2 at 2000 mA g^{-1}.

To gain further insight into the improved electrochemical performance of α-Fe_2O_3@TiO_2 hybrid for LIBs, electrochemical impedance spectroscopy (EIS) measurements of the three electrodes were carried out at around 2.3 V (room temperature) on cells comprising the samples as the working electrode versus Li after cycling for different cycles. The corresponding three-dimensional Nyquist plots are shown in Fig. 8. All the Nyquist plots are similar to each other, with a semicircle at high-medium frequency and an inclined straight line at low frequency. The EIS data are analyzed by fitting to an equivalent electrical circuit (shown in Fig. 8d), where R_s as the ohmic resistance (total resistance of the electrolyte, separator, and electrical contacts), R_{ct} as the charge transfer resistance, W as the Warburg impedance of Li^+ diffusion into the active materials, and *CPE* is the constant phase-angle element which involves double layer capacitance. Nyquist plots are fitted as the red smooth curves and the fitted impedance data are listed in Table 2. The fitting patterns are well agreed with the experimental EIS data. From Table 2, after the 1^{st} cycle, the R_s (2.163 Ω) and R_{ct} (98.49 Ω) of α-Fe_2O_3@TiO_2 are slightly higher than those of α-Fe_2O_3 (1.807 Ω, 61.24 Ω) because of the relatively low electronic conductivity of TiO_2, however, the high stable structure of TiO_2 makes them undergo a little increase with cycling. These results demonstrate that the α-Fe_2O_3@TiO_2 electrode has high stability, lower polarization and faster Li^+ diffusion, verifying excellent electrochemical

365 performance as the promising anode material of LIBs.

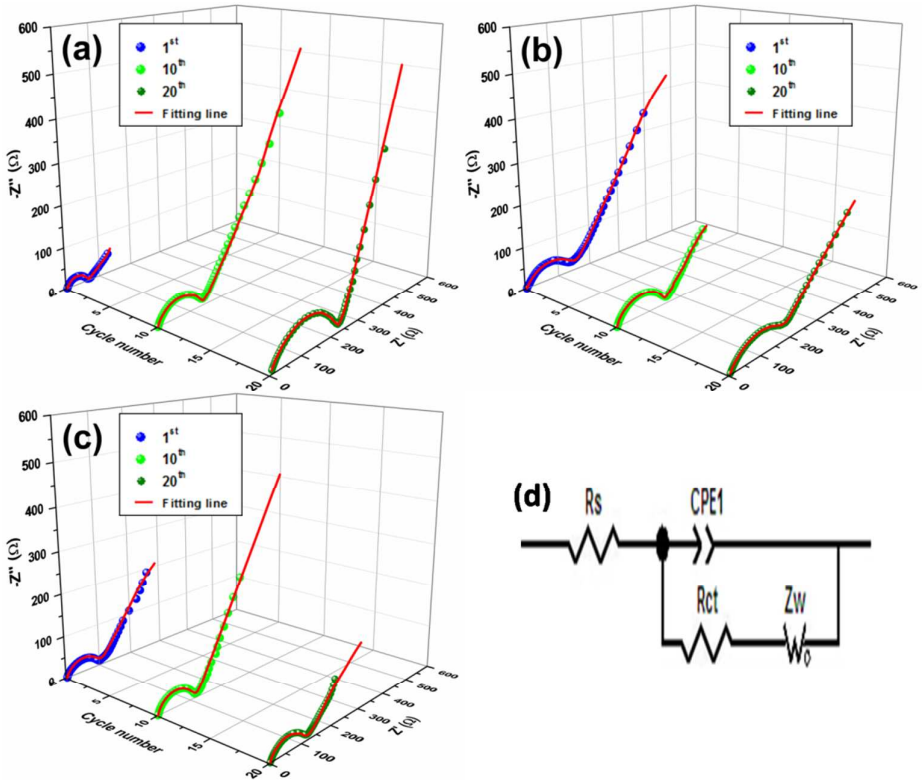

366

367 **Fig. 8** Three-dimensional Nyquist plots for (a) α-Fe_2O_3, (b) TiO_2 and (c) α-Fe_2O_3@TiO_2 electrodes

368 after different cycles at a current density of 100 mA g^{-1} with a scan rate of 0.01 mV s^{-1}. (d) The

369 equivalent circuit used for fitting the experimental EIS data.

370 **Table 2** R_s and R_{ct} values obtained from equivalent circuit fitting of experimental data for three

371 electrodes in LIBs.

samples	R_s (Ω)			R_{ct} (Ω)		
	1st	10th	20th	1st	10th	20th
α-Fe_2O_3	1.807	3.019	5.163	61.24	133.1	229.7
TiO_2	3.030	3.464	4.069	138.6	148.2	200.0
α-Fe_2O_3@TiO_2	2.163	2.284	2.447	98.49	103.7	111.6

372 In terms of the effect of TiO_2 on the structure of α-Fe_2O_3@TiO_2 composite, the

TEM images of the α-Fe_2O_3 and α-Fe_2O_3@TiO_2 electrodes after 100 cycles are shown in Fig. 9. As being seen, the morphology of α-Fe_2O_3 looks seriously aggregated and pulverized, while α-Fe_2O_3@TiO_2 retains well its hollow porous nanosphere architecture by means of the protection of TiO_2, except that its volume increases a little after repeated Li insertion/extraction processes.

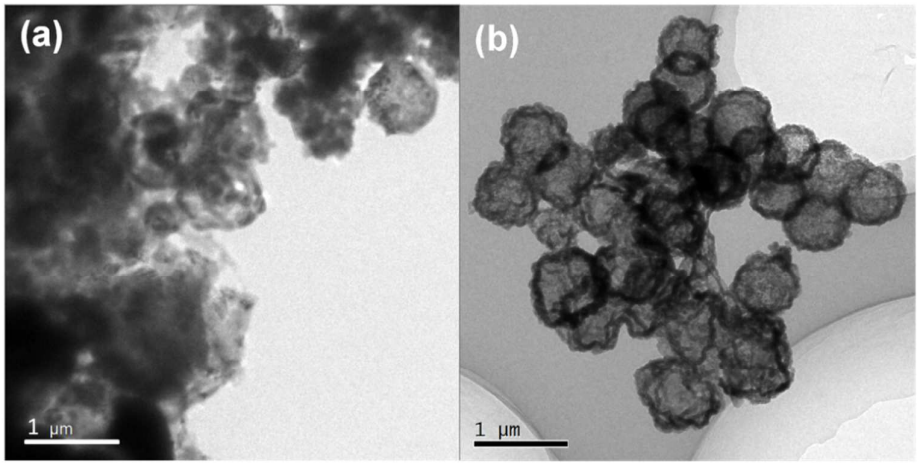

Fig. 9 TEM images of (a) α-Fe_2O_3 and (b) α-Fe_2O_3@TiO_2 electrodes after 100 cycles.

3.3 Electrochemical analysis of sodium ion batteries.

The electrochemical performance for the prepared samples was further tested in coin-type sodium half cells. In order to reveal the Na^+ insertion/extraction behavior of α-Fe_2O_3@TiO_2, cyclic voltammetry (CV) and galvanostatic discharge/charge cycling performance were investigated between 0.01 and 3.0 V at a scan rate of 0.1 mV s^{-1}. Fig. 10a shows the typical CV curves for α-Fe_2O_3@TiO_2 electrode. In the first cathodic scan, a weak peak at ~1.0 V corresponds to the electrochemical reduction process of α-Fe_2O_3 with Na to form $Na_xFe_2O_3$, followed by another weak peak at ~0.5 V, which is ascribed to further reduction of $Na_xFe_2O_3$ and reduction process for TiO_2, as well as SEI films formation.[35, 48] Meanwhile, in the anodic process, a peak

positioned at ~1.6 V is assigned to the reversible oxidation of Fe^0 to Fe^{3+}.[7, 35] The overall electrochemical reaction for α-Fe_2O_3 can be expressed as:

$$Fe_2O_3 + 6Na \leftrightarrow 2Fe + 3Na_2O \quad (5)$$

In the subsequent cycles, it is worth noting that the anodic (~0.85 and ~1.75 V) and cathodic (~0.7 V) peaks become remarkable, and the CV curves obviously overlap well, suggesting a highly reversible reaction of α-Fe_2O_3@TiO_2 with Na. This result is in agreement with the discharge-charge measurement. As shown in Fig. 10b, the initial discharge capacity of α-Fe_2O_3@TiO_2 is 825 mA h g^{-1} without an obvious potential plateau shown in LIBs probably due to the presence of small nanoparticles of α-Fe_2O_3,[49] as well as the large size, heavy mass, and poor mobility of Na^+,[7, 50] and it drops rapidly to 458 mA h g^{-1} in the second cycle. Fortunately, the capacity reduces slightly during the following cycles and still remains a high capacity of 267 mA h g^{-1} after 300 cycles. In contrast, Wang et al.[51] fabricated hollow α-Fe_2O_3 nanosphere by carbon-template method delivers only 248 mA h g^{-1} at 50 mA g^{-1} over 20 cycles.

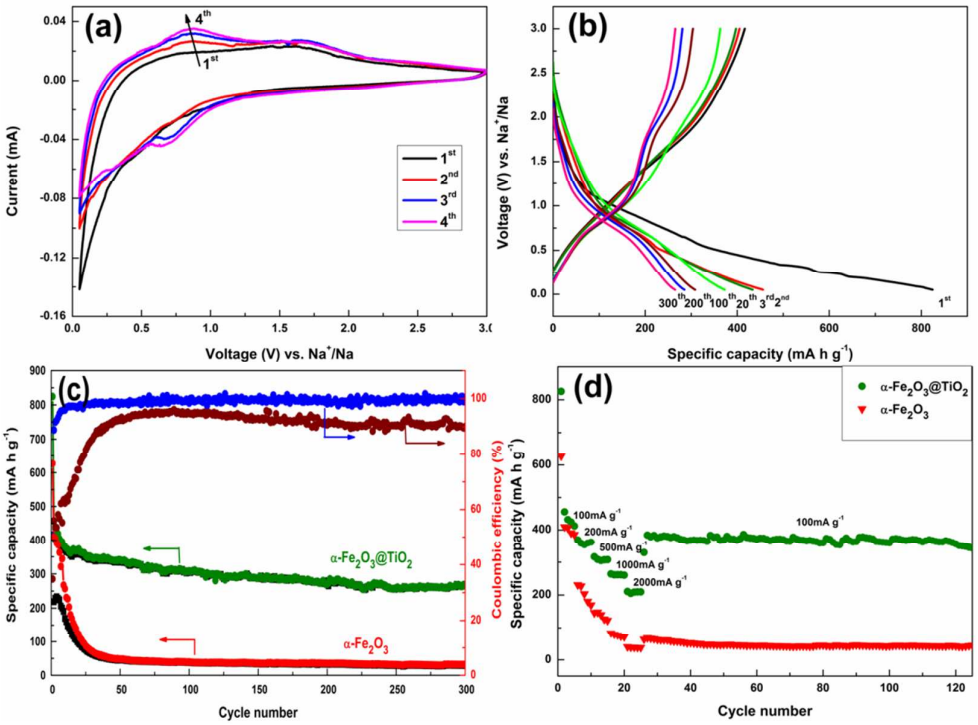

Fig. 10 (a) CV curves and (b) charge-discharge profiles of α-Fe_2O_3@TiO_2 electrode between 0.01 and 3.0 V at a scan rate of 0.1 mV s^{-1}. (c) Cycling performance and coulombic efficiency of α-Fe_2O_3@TiO_2 (green and blue) and α-Fe_2O_3 (red and wine) electrodes at a current density of 100 mA g^{-1}. (d) Rate performance of α-Fe_2O_3@TiO_2 and α-Fe_2O_3 electrodes at various current densities from 100 to 2000 mA g^{-1}.

Fig. 10c compares the cycling performance and coulombic efficiencies (CEs) for α-Fe_2O_3@TiO_2 and α-Fe_2O_3 samples at 100 mA g^{-1} between 0.01 and 3.0 V. Apparently, although the initial specific capacity and CE for α-Fe_2O_3@TiO_2 (825 mA h g^{-1}, 50.5%) are much higher than those of α-Fe_2O_3 (627 mA h g^{-1}, 34.9%), it is inevitably lower than those in LIBs maybe caused by some forms of irreversible trapping and larger size of Na. Compared with the rapid capacity fading of α-Fe_2O_3, the α-Fe_2O_3@TiO_2 electrode exhibits significantly enhanced cyclability benefiting from not only the unique crystal structure of TiO_2 coating layer, which provides

possible interstitial sites for Na accommodation and suitable sized pathways for Na diffusion, but also the preponderant porous hollow structure, which creates extra space for Na storage and buffers the larger volume expansion during cycling, thus leading a high structural stability and satisfactory cycling performance for SIBs.

The rate capability for α-Fe_2O_3 and α-Fe_2O_3@TiO_2 electrode at different current densities from 100 to 2000 are shown in Fig. 10d. It is evident that the α-Fe_2O_3@TiO_2 owns a notably higher capacity and improved rate performance in comparison to α-Fe_2O_3. Even though it is cycled with a high current density of 2000 mA g^{-1}, it still delivers discharge capacity of 210 mA h g^{-1} (40 mA h g^{-1} for α-Fe_2O_3). After cycling at such a large current density, the capacity still can be observed (~370 mA h g^{-1}) as high as its original value at 100 mA g^{-1}, suggesting a strong tolerance toward high rate cycling.

As tested in LIBs, the EIS was also conducted at around 2.0 V (room temperature) on cells with α-Fe_2O_3@TiO_2 electrode versus Na at a cutoff voltage window of 0.01-3.0 V after the 1st, 10th and 20th cycles for SIBs. The EIS experiment and data processing are similar to those in LIBs. As can be seen from Fig. 11, the fitted plots are expressed as the red smooth lines and well consistent with experimental data. The corresponding fitted impedance data are listed in Table 3. Obviously, the R_{ct} of α-Fe_2O_3@TiO_2 after the 1st, 10th and 20th cycles are 180.1, 329.2 and 399.6 Ω, respectively, showing less increase with cycling; the R_s values also display slight difference. Apparently, these results are still inferior to those in LIBs, suggesting the existence of some drawbacks and obstacles of SIBs for application,

which include sluggish kinetics of Na, high polarization, inappropriate electrolyte and membrane.[52] Nonetheless, above results show primarily that the porous hollow α-Fe_2O_3@TiO_2 sphere will be a promising anode electrode for SIBs.

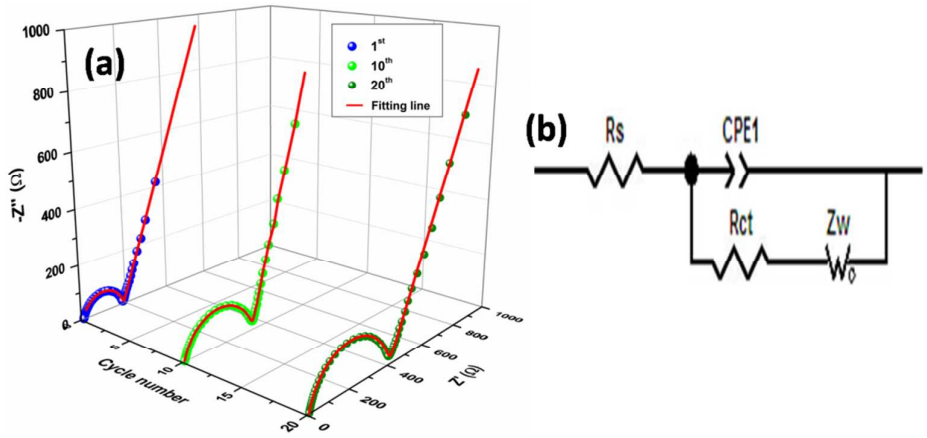

Fig. 11 (a) Three-dimensional Nyquist plots for α-Fe_2O_3@TiO_2 electrode after different cycles at a current density of 100 mA g^{-1} with a scan rate of 0.01 mV s^{-1}. (b) The equivalent circuit used for fitting the experimental EIS data.

Table 3 R_s and R_{ct} values obtained from equivalent circuit fitting of experimental data for α-Fe_2O_3@TiO_2 in SIBs.

sample	R_s (Ω)			R_{ct} (Ω)		
	1st	10th	20th	1st	10th	20th
α-Fe_2O_3@TiO_2	9.171	10.81	11.03	180.1	329.2	399.6

The exceptional electrochemical performance has already confirmed that the α-Fe_2O_3@TiO_2 hollow spheres will be an appealing anode material for both LIBs and SIBs. Several factors make great contribution to it, including: (1) the porous hollow structure with high specific surface area makes active material have efficient contact with electrolyte, and possess extra space for the storage of alkalis (Li and Na); (2) the

void space in hollow structure is able to buffer the large volume variation during cycling and prevent the electrode from pulverization and aggregation; (3) the addition of TiO_2 acts as a buffer layer to accommodate the volume change of α-Fe_2O_3 due to its unexceptionable structure stability; (4) the 3D network crystallographic structure of TiO_2 offers empty zigzag channels to provide interstitial sites and suitable sized pathways for alkalis (Li and Na); (5) Li could insert into TiO_2 during the initial discharge process at 1.7 V (vs Li^+/Li), leading to the formation of Li_xTiO_2, where the Ti^{3+} in Li_xTiO_2 is expected to enhance the overall electronic conductivity of the electrode material.

4. Conclusion

In summary, the α-Fe_2O_3@TiO_2 hybrid composite with porous hollow structure and TiO_2 coating has been successfully designed and synthesized by a facile carbon-template method. Compared with hollow α-Fe_2O_3, the α-Fe_2O_3@TiO_2 hybrid nanosphere with rational structure combining with the structural stability of TiO_2 shows excellent electrochemical features in terms of high specific capacity, long cycle life, excellent rate capability, and satisfactory initial coulombic efficiency. The dramatically improved electrochemical performance can be attributed to a synergetic effect between α-Fe_2O_3 and TiO_2 as well as the unique feature of porous hollow structure, which contributes to greatly enhanced diffusion kinetics and structural stability for alkalis (Li and Na). The synthetic strategy of such nanoarchitecture material provides a new pathway to fabricate other oxides heterostructures, thus creating new opportunities for designing a wide range of high-performance LIBs and

476 SIBs electrode materials.

477 Acknowledgements

478 This work is supported financially by the National Natural Science Foundation
479 of China under project No. 51472211, Scientific and Technical Achievement
480 Transformation Fund of Hunan Province under project No. 2012CK1006, Key Project
481 of Strategic New Industry of Hunan Province under project No. 2013GK4018 and the
482 Natural Science Foundation of Hunan Province under project No 2015JJ6103. Q. Wei
483 gratefully acknowledges the scholarship from China Scholarship Council (CSC).

484 References

485 1 M. Armand and J.-M. Tarascon, *Nature*, 2008, **451**, 652.

486 2 L. Ji, Z. Lin, M. Alcoutlabi and X. Zhao, *Energy Environ. Sci.*, 2011, **4**, 2682.

487 3 J. B. Goodenough and Y. Kim, *Chem. Mater*., 2010, **22**, 587.

488 4 C. Liu, F. Li, L. Ma and H. Cheng, *Adv. Mater.*, 2010, **22**, E28.

489 5 P. Poizot and F. Dolhem, *Energy Environ. Sci.*, 2011, **4**, 2003.

490 6 M. D. Slater, D. Kim, E. Lee and C. S. Johnson, *Adv. Funct. Mater.*, 2013, **23**, 947.

491 7 N. Zhang, X. Han, Y. Liu, X. Hu, Q. Zhao and J. Chen, *Adv. Energy Mater.*, 2015, **5**.

492 8 J. Song, Z. Yu, M. L. Gordin, S. Hu, R. Yi, D. Tang, T. Walter, M. Regula, D. Choi,
493 X. Li, A. Manivannan and D. Wang, *Nano Lett.*, 2014, **14**, 6329.

494 9 Z. Wang, D. Luan, S. Madhavi, Y. Hu and X. W. Lou, *Energy Environ. Sci.*, 2012, **5**,
495 5252.

496 10 L. Lang and Z. Xu, *ACS Appl. Mater. Interfaces*, 2013, **5**, 1698.

497 11 Y. Zhao, J. Li, Y. Ding and L. Guan, *Chem. Commun*., 2011, **47**, 7416.

12 J. Zhang, K. Wang, Q. Xu, Y. Zhou, F. Cheng and S. Guo, *ACS Nano*, 2015, **9**, 3369.

13 G. Zhang, H. Wu, T. Song, U. Paik and X. W. Lou, *Angew. Chem. Int. Ed.*, 2014, **53**, 12590.

14 D. Li, Q. Qin, X. Duan, J. Yang, W. Guo and W. Zheng, *ACS Appl. Mater. Interfaces*, 2013, **5**, 9095.

15 J. Choi, W.-S. Kim and S.H. Hong, *Nano Res.*, 2014, **7**, 1128.

16 H. Xiao, Y. Xia, W. Zhang, H. Huang, Y. Gan and X. Tao, *J. Mater. Chem. A*, 2013, **1**, 2307.

17 W. Zhou, C. Cheng, J. Liu, Y. Y. Tay, J. Jiang, X. Jia, J. Zhang, H. Gong, H. H. Hng, T. Yu and H. J. Fan, *Adv. Funct. Mater.*, 2011, **21**, 2439.

18 Q.Q. Xiong, X.H. Xia, J.P. Tu, J. Chen, Y.Q. Zhang, D. Zhou, C.D. Gu and X.L. Wang, *J. Power Sources*, 2013, **240**, 344.

19 J.-M. Jeong, B. G. Choi, S. C. Lee, K. G. Lee, S.-J. Chang, Y.-K. Han, Y. B. Lee, H. U. Lee, S. Kwon, G. Lee, C.-S. Lee and Y. S. Huh, *Adv. Mater.*, 2013, **25**, 6250.

20 X. Gu, L. Chen, Z. Ju, H. Xu, J. Yang and Y. Qian, *Adv. Funct. Mater.*, 2013, **23**, 4049.

21 X. Zhang, H. Chen, Y. Xie and J. Guo, *J. Mater. Chem. A*, 2014, **2**, 3912.

22 G. Zhang, H. B. Wu, T. Song, U. Paik and X. W. Lou, *Angew. Chem. Int. Ed.*, 2014, **53**, 1.

23 Y.-Q. Wang, L. Gu, Y.-G. Guo, H. Li, X.-Q. He, S. Tsukimoto, Y. Ikuhara and L.-J. Wan, *J. Am. Chem. Soc.*, 2012, **134**, 7874.

24 J. S. Chen, Y. L. Tan, C. M. Li, Y. L. Cheah, D. Y. Luan, S. Madhavi, F. Y. C. Boey, L. A. Archer and X. W. Lou, *J. Am. Chem. Soc.*, 2010, **132**, 6124.

25 C. Wu, P. Yin, X. Zhu, C. O. Yang and Y. Xie, *J. Phys. Chem. B*, 2006, **110**, 17806.

26 L. Tang, Y. Wang, Y. Li, H. Feng, J. Lu and J. Li, *Adv. Funct. Mater.*, 2009, **19**, 2782.

27 G. K. Pradhan and K. M. Parida, *ACS Appl. Mater. Interfaces*, 2011, **3**, 317.

28 H. Xia, W. Xiong, C. K. Lim, Q. Yao, Y. Wang and J. Xie, *Nano Res.*, 2014, **7**, 1797.

29 Y. Luo, J. Luo, J. Jiang, W. Zhou, H. Yang, X. Qi, H. Zhang, H. J. Fan, D. Y. W. Yu, C. M. Li and T. Yu, *Energy Environ. Sci.*, 2012, **5**, 6559.

30 J. Luo, X. Xia, Y. Luo, C. Guan, J. Liu, X. Qi, C. F. Ng, T. Yu, H. Zhang and H. J. Fan, *Adv. Energy Mater.*, 2013, **3**, 737.

31 Y. Fu, X. Wang, H. Wang, Y. Zhang, X. Yang and H. Shu, *RSC Adv.*, 2015, **5**, 14531.

32 H. Wang, G. Wang, S. Yuan, D. Ma, Y. Li and Y. Zhang, *Nano Res.*, 2015

33 J. Zhu, Z. Yin, D. Yang, T. Sun, H. Yu, H. E. Hoster, H. H. Hng, H. Zhang and Q. Yan, *Energy Environ. Sci.*, 2013, **6**, 987.

34 J. S. Cho, Y. J. Hong and Y. C. Kang, *ACS Nano*, 2015.

35 Z. Yan, L. Liu, J. Tan, Q. Zhou, Z. Huang, D. Xia, H. Shu, X. Yang and X. Wang, *J. Power Sources*, 2014, **269**, 37.

36 Z. Yang, Q. Meng, Z. Guo, X. Yu, T. Guo and R. Zeng, *J. Mater. Chem. A*, 2013, **1**, 10395.

37 B. Philippe, M. Valvo, F. Lindgren, H. Rensmo and K. Edström, *Chem. Mater.*, 2014, **26**, 5028.

38 J. Guo, L. Chen, G. Wang, X. Zhang and F. Li, *J. Power Sources*, 2014, **246**, 862.

39 X. Huang, H. Yu, J. Chen, Z. Lu, R. Yazami and H. H. Hng, *Adv. Mater.*, 2014, **26**, 1296.

40 X. Lv, J. Deng, J. Wang, J. Zhong and X. Sun, *J. Mater. Chem. A*, 2015, **3**, 5183.

41 Y. Li, Y. Hu, H. Jiang, X. Hou and C. Li, *CrystEngComm*, 2013, **15**, 6715.

42 W. Li, J. Yang, Z. Wu, J. Wang, B. Li, S. Feng, Y. Deng, F. Zhang and D. Zhao, *J. Am. Chem. Soc.*, 2012, **134**, 11864.

43 G.Wang, H. Wang, S. Cai, J. Bai, Z. Ren and J. Bai, *J. Power Sources*, 2013, **239**, 37.

44 H.-S. Lim,Y.-K. Sun and K.-D. Suh, *J. Mater. Chem. A*, 2013, **1**, 10107.

45 J. S. Cho, Y. J. Hong and Y. C. Kang, *ACS Nano*, 2015, **9**, 4026.

46 S. Xu, C. M. Hessel, H. Ren, R. Yu, Q. Jin, M. Yang, H. Zhao and D. Wang, *Energy Environ. Sci.*, 2014, **7**, 632.

47 G. Du, N. Sharma, V. K. Peterson, J. A. Kimpton, D. Jia and Z. Guo, *Adv. Funct. Mater.*, 2011, **21**, 3990.

48 Y. Xu, E. M. Lotfabad, H. Wang, B. Farbod, Z. Xu, A. Kohandehghan and D. Mitlin, *Chem. Commun.*, 2013, **49**, 8973.

49 Z. Jian, B. Zhao, P. Liu, F. Li, M. Zheng, M. Chen, Y. Shi and H. Zhou, *Chem. Commun.*, 2014, **50**, 1215.

50 J. Chen, L. N. Xu, W. Y. Li and X. L. Gou, *Adv. Mater.*, 2005, **17**, 582.

564 51 S. Wang, W. Wang, P. Zhan and S. Jiao, *Chemelectrochem*, 2014, **1**, 1636.

565 52 H. Pan, Y.-S. Hu and L. Chen, *Energy Environ. Sci.*, 2013, **6**, 2338.